



Sentinel-1 Detection of Ice Slabs on the Greenland Ice Sheet

Riley Culberg¹, Roger J. Michaelides², and Julie Z. Miller³

¹Department of Earth and Atmospheric Sciences, Cornell University

²Department of Earth, Environmental, and Planetary Sciences, Washington University in St. Louis

³Earth Science and Observation Center, Cooperative Institute for Research in Environmental Sciences, University of Colorado Boulder

Correspondence: Riley Culberg (rtculberg@cornell.edu)

Abstract. Ice slabs are multi-meter thick layers of refrozen ice that limit meltwater storage in firn, leading to enhanced surface runoff and ice sheet mass loss. To date, ice slabs have largely been mapped using airborne ice-penetrating radar, which has limited spatial and temporal coverage. This makes it difficult to fully assess the current extent and continuity of ice slabs or to validate predictive models of ice slab evolution that are key to understanding their impact on Greenland's surface mass balance. Here, for the first time, we map the extent of ice slabs and similar superimposed ice facies across the entire Greenland Ice Sheet at 500 m resolution using dual-polarization Sentinel-1 (S-1) synthetic aperture radar data collected in winter 2016-2017. The S-1 inferred ice slab extent is in excellent agreement with ice-penetrating radar ice slab detections from spring 2017, as well as the extent of the visible runoff zone as mapped from optical imagery. Our results show that ice slabs are nearly continuous around the entire margin of the ice sheet, including regions in Southwest Greenland where ice slabs have not been previously identified. The algorithm developed here also lays the groundwork for long-term monitoring of ice slab expansion with current and future C-band satellite systems and highlights the added value of future L-band missions for near-surface studies in Greenland.

1 Introduction

Over the last two decades, more than half of mass loss from the Greenland Ice Sheet (GrIS) has come from the runoff of surface meltwater (Van Den Broeke et al., 2009; Enderlin et al., 2014; Mougnot et al., 2019), and surface processes are projected to remain the dominant contributor to Greenland's sea level contribution over the next century (Fox-Kemper et al., 2021). By extension, much of the uncertainty in future mass loss from the ice sheet can also be ascribed to uncertainty in surface processes (Fox-Kemper et al., 2021). One process that remains poorly constrained is the development and expansion of ice slabs in firn near the equilibrium line. Ice slabs are multi-meter thick layers of refrozen ice that form just below the surface (Machguth et al., 2016) and can be horizontally continuous over tens of kilometers (MacFerrin et al., 2019). As a result, ice slabs are largely impermeable and limit the vertical percolation of meltwater into the underlying relict firn, leading to a rapid transition from retention to runoff as they form (Machguth et al., 2016; MacFerrin et al., 2019; Tedstone and Machguth, 2022). To date, ice slabs have primarily been mapped using Operation IceBridge (OIB) airborne ice-penetrating radar surveys, as these data directly resolve the vertical structure of the subsurface and can distinguish homogeneous refrozen ice bodies from



25 lower density firn (MacFerrin et al., 2019; Jullien et al., 2023). These data have shown that ice slabs dominate the wet snow zone along the western, northern, and northeastern coasts of Greenland. The southeast basin is the only major region where no ice slabs have been detected, due to the high snow accumulation rate that insulates subsurface liquid water from refreezing and preferences the formation of perennial firn aquifers (Forster et al., 2014; Munneke et al., 2014).

While the OIB data have provided critical insights into ice slab extent across the GrIS, these data are significantly limited in both space and time. Data are only available directly beneath the aircraft track, and collection was limited to a moderate number of flight lines in spring (typically April or May) each year from 2011-2014 and 2017-2018, along with a few additional flights over the wet snow zone in 2010. These gaps in coverage lead to a number of issues. In many regions, the upper limit of the ice slabs is poorly defined, due to a lack of flights perpendicular to the coastline, and there are some areas, most notably in southern Greenland and on peripheral ice caps, where there is insufficient flight coverage to assess whether ice slabs are even present. Even in regions of good coverage, there are typically 5-20 km gaps between flight lines. As a result, the full extent of ice slabs on the GrIS remains poorly defined and it has been difficult to fully assess the km-scale continuity of this facie. Additionally, there are very few repeated flights that were flown perpendicular to the coastline, which are required to robustly assess the inland expansion of ice slabs from year to year. Jullien et al. (2023) showed that some growth occurred between the period from 2010-2012 to 2017-2018, but the spatial resolution of that analysis was coarse and limited by the need to aggregate multiple years of data to achieve reasonable coverage of the whole ice sheet. With the end of the OIB mission in 2019, there is no new ice-penetrating radar data to improve these time series or assess the impact of more recent heavy melt seasons, which included the first high elevation rain event, such as 2019, 2021, and 2023 (Tedesco and Fettweis, 2020; Harper et al., 2023; Box et al., 2023).

These spatial and temporal gaps significantly impede our ability to assess the impact of ice slab development and expansion on the current and future mass balance of the GrIS. For example, MacFerrin et al. (2019) parameterized ice slab extent as a function of the ten-year running mean of local excess melt and applied this parameterization to an ensemble of regional climate models to predict that ice slab expansion would add 7-74 mm of additional sea level rise by 2100. However, this excess melt threshold was tuned by matching the modeled ice slab extent to the aggregate observed extent from 2010-2014 (MacFerrin et al., 2019). As a result, it remains unclear whether the temporal evolution of ice slabs in this model accurately captures the true pace of ice slab growth. As firn models continue to improve, there are many opportunities to implement more physics-based estimates of ice slab expansion and runoff contributions, but in the absence of validating data, significant uncertainties in future projections will remain.

The only clear mechanism for mapping ice slab extent across the entire ice sheet at high resolution (~1 km or better) on an annual or better basis is to use satellite microwave remote sensing systems. In fact, ice slabs have been mapped from space using the L-band radiometer onboard the Soil Moisture Active Passive (SMAP) mission by Miller et al. (2022a). However, there are significant limitations to this approach. In particular, the instrument resolution is approximately 30 km (Miller et al., 2022a), making it difficult to clearly define the inland extent of the ice slabs or capture expansion on the order of a few kilometers or less per a year. Additionally, although rough estimates of the interannual variability are given, this algorithm aggregates ~5 years of radar data to create a single estimate of ice slab extent (Miller et al., 2022a), which limits its use for generating long



60 time series. There are also notable discrepancies between the SMAP and OIB ice slab extents, particularly in the Northwest where SMAP fails to detect large swaths of the OIB-detected ice slabs, and in the North and Northeast where SMAP places the ice slabs at higher elevations than the OIB data (see Figure 11).

An alternate approach is to use active synthetic aperture radar systems such as the European Space Agency's (ESA) Sentinel-1 (S-1) series satellites. Since C-band radio waves penetrate roughly 5-15 meters into snow, firn, and ice, depending on the local physical and dielectric properties (Rignot et al., 2001; Hoen, 2001; Fischer et al., 2019), the depth-integrated surface echo measured by the instrument contains information about the near-surface structure. In Extra Wide Swath mode, Sentinel-1 covers the entire GrIS approximately every 10 days with a spatial resolution of 20 x 40 meters and a full catalog of data available from late 2014 to the present day. With the anticipated launches of Sentinel-1C & D, the data record is projected to continue uninterrupted through at least the early 2030s. Therefore, Sentinel-1 could not only provide the first pan-Greenland mapping of ice slabs, but such an algorithm would open the door to long-term monitoring of ice slab expansion, potentially covering close to two decades of observations. Here, we develop an algorithm to map refrozen ice facies on the Greenland Ice Sheet using dual polarization Extra Wide swath Sentinel-1 measurements of radar backscatter in conjunction with calibration data from ice-penetrating radar observations.

2 Electromagnetic Interactions in Firn

75 On ice sheets, mean firn density increases exponentially with depth as it compacts under its own weight (Bader, 1954; Herron and Langway, 1980). In the percolation zone, the structure is further modified by the infiltration and refreezing of surface meltwater that forms ice lenses and ice pipes (Benson, 1962). Ice lenses are horizontal sheets of refrozen solid ice that may be up to a few tens of cms thick and extend laterally for a few meters (Benson, 1962; MacFerrin et al., 2019), while ice pipes are vertical refrozen conduits that represent preferential infiltration pathways connecting these ice lenses (Marsh and Woo, 1984; Pfeffer and Humphrey, 1998; Humphrey et al., 2012). The proportion of the firn occupied by these refreeze features generally increases with decreasing elevation and increasing melt-to-accumulation ratio (Harper et al., 2012; Machguth et al., 2016). In the extreme, consistent excess melting may anneal these ice lenses together into multi-meter thick ice slabs that form in the wet snow zone (MacFerrin et al., 2019; Machguth et al., 2016). The wet snow facies eventually transition to the ablation zone via a region of superimposed ice facies, where the near-surface ice is formed by refreezing within the annual accumulation (Benson, 1962). At the lowest elevations, where annual melting consistently exceeds accumulation, the ice sheet transitions to the bare ice ablation zone composed of homogeneous meteoric ice that is exposed at the surface via horizontal advection and ablation.

These near-surface structural variations with elevation lead to commensurate changes in the dominant electromagnetic scattering mechanisms. In the percolation zone, radar echoes are thought to be dominated by volume scattering from embedded ice features on the scale of a few wavelengths (Fahnestock et al., 1993; Jezek et al., 1994; Rignot, 1995; Baumgartner et al., 1999; Langley et al., 2009), making the GrIS percolation zone one of the most radio bright regions on Earth (Swift et al., 1985; Rignot et al., 1993; Jezek et al., 1994). Past work has successfully modeled the observed percolation zone backscatter at C-band as volume scattering from randomly oriented cylinders (Rignot, 1995). This volume scattering dominated regime

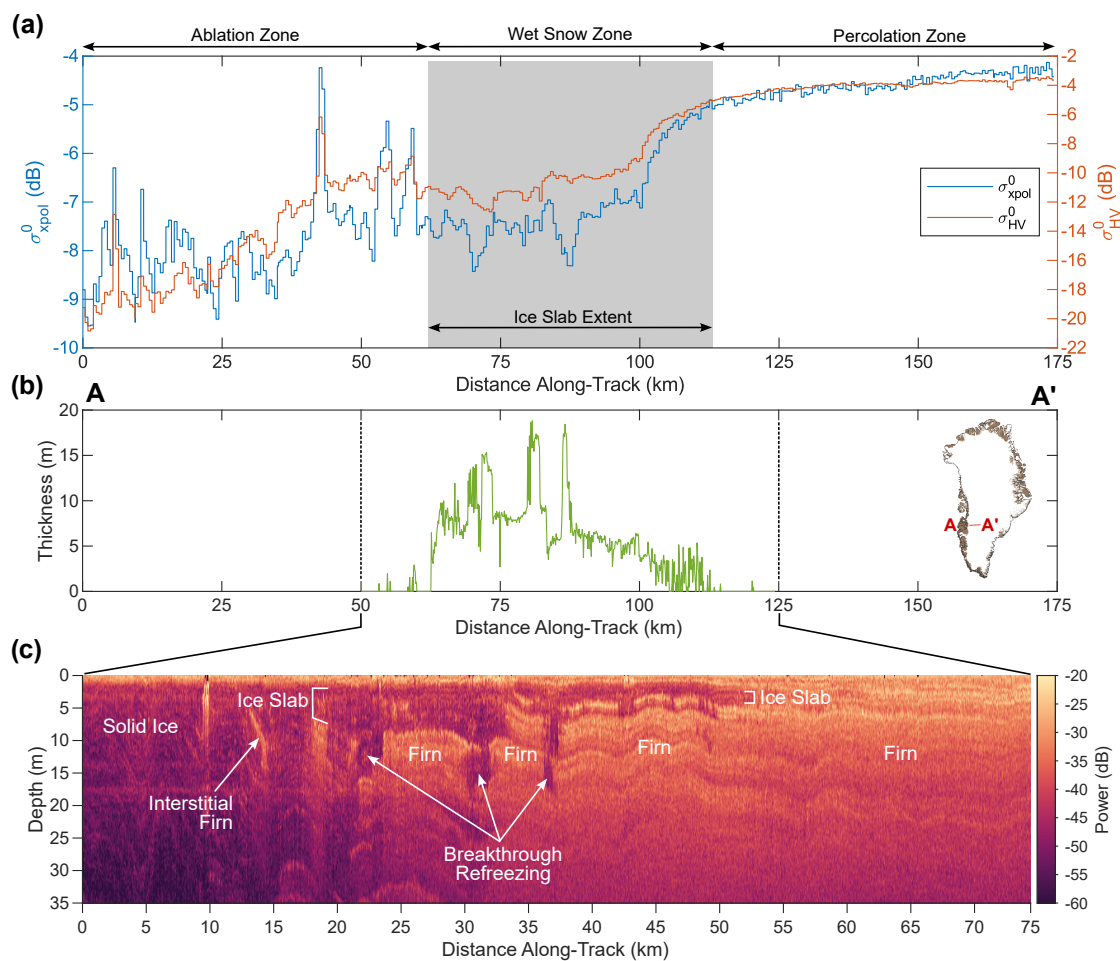


Figure 1. Radar signatures of ice slabs along a transect in Southwest Greenland. (Contains modified Copernicus Sentinel data 2016-2017, processed by ESA.) a) Sentinel-1 σ_{HV}^0 is shown in red and the cross-pol backscatter ratio, $\sigma_{xpol}^0 = \sigma_{HV}^0 - \sigma_{HH}^0$ is shown in blue. The gray region denotes where ice slabs have been detected with ice-penetrating radar (Culberg et al., 2022b). b) Ice slab thickness along the transect as measured with ice-penetrating radar (Culberg et al., 2022b). There is a rapid, down-flow decrease in σ_{xpol}^0 as the ice slab thickens, with the backscatter saturating once the ice slab reaches a thickness of around 7 m. The inset map (Gerrish, 2020; Morlighem et al., 2017) shows the location of this transect in Southwest Greenland. c) Radargram from April 2015 collected by the Ultrawideband MCoRDS system (Paden et al., 2014a) showing the subsurface structure in the region where ice slabs have been detected. In the percolation zone, the structure is dominated by layered firn with strong scattering from small embedded ice features. In the wet snow zone, a thick layer of homogeneous refrozen ice with low backscatter overlies relict firn. In the ablation zone, only solid ice remains and there is relatively low backscatter at all depths due to the absence of density contrasts in the subsurface.

also leads to significant depolarization of the incident wave and a large radar cross-section in the cross-polarized (HV or VH) channels (Jezek et al., 1993; Rignot, 1995; Langley et al., 2007; Barzycka et al., 2019). By contrast, scattering in the bare ice



95 ablation zone is dominated by rough surface scattering at the air-ice interface, with relatively little volume scattering since
heterogeneities such as air bubbles are significantly smaller than the C-band wavelength (Langley et al., 2007, 2009; Barzycka
et al., 2019). As a result, the radar cross section of the ablation zone is relatively small and little depolarization occurs, so the
echoes are dominated by co-polarized (HH or VV) returns (Langley et al., 2007, 2009). Numerous papers have mapped glacier
facies on Arctic ice caps and mountain glaciers based on these characteristic changes in backscatter (Partington, 1998; Long
100 and Drinkwater, 1994; Barzycka et al., 2019). For example, Langley et al. (2008) demonstrated that on Kongsvegen Glacier
in Svalbard, the boundaries between firn, superimposed ice, and glacier ice could be mapped in C-Band ENVISAT SAR data
from the ~ 5 dB change in backscatter between each region, with ground-penetrating radar used to validate the mapping.

Ice slab regions likely represent an intermediate scattering regime between the percolation zone and superimposed ice or
ablation zones, with a balance of both surface and volume scattering. Nadir-looking airborne radar sounding measurements
105 show that ice slabs are characterized by strong reflections from their upper and lower interfaces, but very low backscatter
within the refrozen ice itself (MacFerrin et al., 2019; Jullien et al., 2023). However, the presence of remnant interstitial firn
layers does lead to overall higher backscatter in these refrozen ice facies than in meteoric ice (Figure 1c). Side-looking synthetic
aperture radar returns from ice slabs display greater surface scattering and lower volume scattering than the percolation zone,
but higher volume scattering than meteoric ice in the lower ablation zone. Figure 1a-b shows an example of this effect along a
110 transect from the ice margin to shallow percolation zone in Southwest Greenland. The percolation zone HV backscatter (σ_{HV}^0)
is consistently about -2 dB, but decays at lower elevations as ice slabs begin to form and thicken, eventually reaching a new
plateau around -11 dB. The ratio of the HV to HH backscatter ($\sigma_{xpol}^0 = \sigma_{HV}^0 - \sigma_{HH}^0$ (in dB)), known as the cross-polarized
backscatter ratio (Ulaby and Long, 2014) or linear backscatter ratio (Rignot, 1995), has been used as a proxy for the ratio
of volume to surface scattering in the Greenland percolation zone (Rignot, 1995) and is also responsive to this change in
115 subsurface structure, decreasing from -4.5 dB to -7.5 dB as ice slabs develop. In this paper, we exploit this reduction in volume
scattering that occurs as ice slabs form to map ice slabs from S-1 C-band winter backscatter measurements.

3 Methods

3.1 Sentinel-1 Backscatter Mosaics

For this analysis, we use Extra Wide Swath (EW) ground range detected (GRD) Sentinel-1A & B data collected in HH and
120 HV polarizations at a center frequency of 5.405 GHz (Agency) over the GrIS from 1 October 2016 to 30 April 2017. Only
 ~ 10 days of data are needed to fully cover the entire ice sheet, but we choose to use the full winter period because the extra
observations allow us to develop a robust mean backscatter map that reduces the influence of temporal variability in scattering
properties, speckle, and variable incidence angles. We expect ice slab extent to be stable during this period since there is
no melt infiltration. We only use winter data because the presence of surface meltwater enhances both the surface dielectric
125 contrast and the near-surface attenuation in water-saturated layers, obscuring the subsurface structure. Due to the huge data
volume, we process these data in Google Earth Engine (GEE) (Gorelick et al., 2017). Data in the GEE S-1 GRD data collection
have undergone thermal noise removal, radiometric calibration, geometric terrain correction, and conversion to dB values in



the Sentinel-1 Toolbox before being posted to the cloud. Unfortunately, these data have not undergone radiometric terrain correction, and it is impossible to fully implement this algorithm in GEE since it requires access to the data in the original radar coordinates. We experimented with applying an angle-based radiometric terrain correction method designed for GEE (Vollrath et al., 2020), but found that it produced little to no change in the backscatter values due to the extremely low surface slopes on most of the ice sheet. Therefore, we do not implement this correction in our final workflow.

With both Sentinel-1A and Sentinel-1B in operation, the exact repeat interval for any point on the ice sheet is 6 days. However, because the EW swath width is 410 km and Greenland is at high latitudes, the coverage is often more frequent. During our 7 month study period, the average number of observations per pixel was 190, or almost one observation per day, with a minimum of 29 and a maximum of 571 observations. The number of observations is highest in the north and around the margins and lowest in the interior southern saddle. Within each observing pass, the incidence angle varies from 18.9° to 47° across swath (Agency), which creates a significant challenge for generating a consistent backscatter mosaic for the entire ice sheet. Particularly in the percolation zone, backscatter varies strongly with incidence angle, which leads to obvious seams between overlapping swaths and spatial variations in backscatter that are attributable to observation geometry rather than physical properties of the ice sheet. Studies using C- and L-band satellite radar scatterometry data often exploit a linear relationship between incidence angle and backscatter to correct for these incidence angle variations across the swath (Long and Drinkwater, 1994; Ashcraft and Long, 2005; Lindsley and Long, 2016; Long and Miller, 2023). However, the coefficients of this linear fit vary with region and time (Lindsley and Long, 2016; Long and Miller, 2023). Therefore to correct for the effects on incidence angle in our mosaic, we fit a linear function to incidence angle vs backscatter on a per-pixel basis using all available images in our study period and then use this relationship to calculate the theoretical backscatter at an incidence angle of 35°. Scatterometer studies have typically corrected their data to an incidence angle of 40°, but here we choose a to correct the data to an incidence angle close to the middle of the S-1 scene. We combine ascending and descending orbits from both satellites to maximize the angular diversity in each pixel for the most robust fit and apply a separate empirical linear to correction to the σ_{HH}^0 and σ_{HV}^0 measurements. In this way, we form a consistent mean winter backscatter image for the entire ice sheet. We then calculate the σ_{xpol}^0 map by subtracting the σ_{HH}^0 map from the σ_{HV}^0 map. Before further analysis, we multi-look each mosaic to 500m square pixels with a boxcar filter and export the data as unsigned 16 bit integers. We also use the BedMachinev3 ice mask to remove pixels in regions without ice (Morlighem et al., 2017).

Figure 2a-b shows the mean winter σ_{HV}^0 and σ_{xpol}^0 mosaics for Greenland in winter 2016-2017. Regions with ice slabs clearly show greater σ_{HV}^0 than the lower ablation zone, but reduced σ_{HV}^0 compared with the percolation zone. Similarly, ice slabs show a lower σ_{xpol}^0 than the percolation zone.

3.2 Excluding the Dry Snow Zone and Firn Aquifer Regions

In order to reduce false positive detection of ice slabs, we exclude regions of the ice sheet that a) experience little to no melting or b) are already known to host firn aquifers. This step is critical because, as can be seen in Figure 2b, both of these regions exhibit low σ_{xpol}^0 values that are on par with what is observed in known ice slab regions. In the dry snow zone, this occurs because the subsurface is dominated by smooth depositional snow layers with little heterogeneity beyond the ice grain scale.

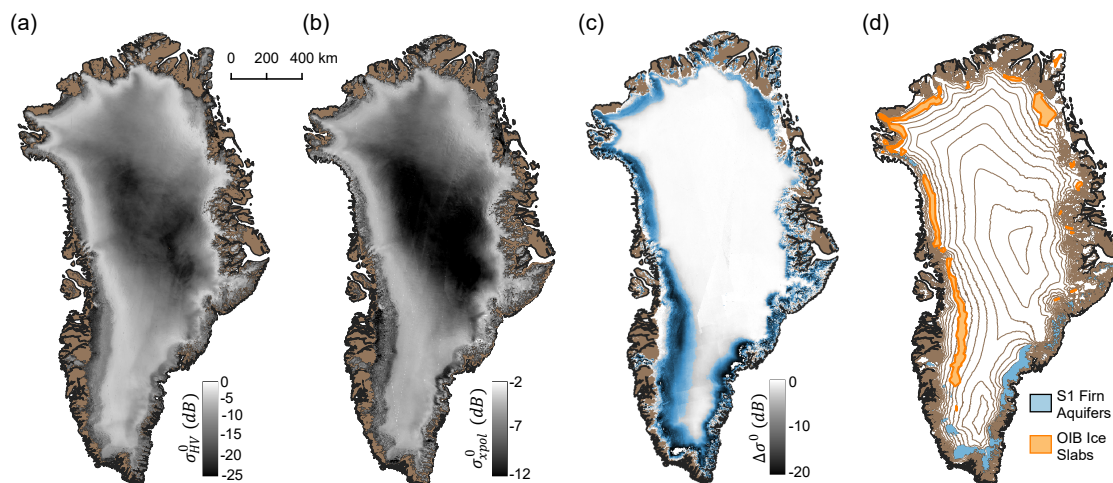


Figure 2. a) Average winter σ_{HV}^0 map at 35° incidence angle covering 1 Oct 2016 - 30 April 2017. b) Average winter σ_{XPOL}^0 map at 35° incidence angle covering 1 Oct 2016 - 30 April 2017. c) Difference between summer and winter HH backscatter ($\Delta\sigma^0$), averaged over 1 Nov 2014 - 31 Aug 2020. We exclude all regions outside the blue overlay from our ice slab analysis, since the minimal change in backscatter between seasons indicates that there is relatively little surface melting in these areas. d) Locations of firn aquifers (blue) detected using Sentinel-1 data from 2014-2019 as published in Brangers et al. (2020). Regions detected as ice slabs with ice-penetrating radar data (Jullien, 2023) are shown in orange for reference. In all panels, the Greenland coastline was produced by the British Antarctic Survey (Gerrish, 2020), the ice mask as part of BedMachine v3 (Morlighem et al., 2017), and the 200 m contours are derived from ArcticDEM (Porter et al., 2018). Panels a-c contain modified Copernicus Sentinel data 2016-2017, originally processed by ESA.

Firn aquifer regions retain liquid meltwater through the winter which leads to increased subsurface absorption and therefore a relatively greater degree of surface scattering, since subsurface volume scattering is suppressed (Brangers et al., 2020; Miller et al., 2022a).

165 To exclude regions with minimal surface melting, we adapt an existing method for mapping wet snow facies in Greenland based on the change in S-1 σ_{HH}^0 between winter and summer (Hu et al., 2022). Much like the classic scatterometer and radiometer algorithms for estimating firn saturation from VV backscatter (Wismann, 2000; Ashcraft and Long, 2006; Hicks and Long, 2011; Miller et al., 2022b), this approach exploits the fact that the enhanced microwave absorption in wet snow leads to a significant reduction in backscatter during the summer when surface melting occurs. We first calculate an average winter σ_{HH}^0 map at 35° incidence angle by applying the linear correction method described in Section 3.1 to aggregated data from 1 Nov - 31 March each year between 2014 and 2020. We calculate an average summer σ_{HH}^0 map at 35° using all observations between 1 July and 31 Aug from 2015-2020 and then calculate the difference between the summer and winter backscatter as $\Delta\sigma^0 = \sigma_{summer}^0 - \sigma_{winter}^0$. We aggregate data over these five years because melt extent varies significantly from year to year and from region to region. This extended time series prevents us from inadvertently excluding areas from analysis due to anomalously low melt extent in any given year. We then choose an empirical threshold to discriminate regions

170

175



with consistent surface melting. Hu et al. (2022) derived a threshold of -7 dB to discriminate between wet snow facies and percolation zone in the $\Delta\sigma^0$ image, based on the distribution of backscatter values observed in Northeast Greenland. However, we find that this threshold is overly aggressive when applied to our average $\Delta\sigma^0$ map and excludes some regions in North Greenland where ice slabs have been observed with ice-penetrating radar. Therefore, we use a threshold of $\Delta\sigma^0 < -4.7$ dB, which is the minimum value that produces a melt region mask which encompasses all OIB ice slab observations from spring 2017. This threshold value falls midway between the Hu et al. (2022) threshold of -7 dB for discriminating wet snow facies and the common threshold of -3 dB for discriminating regions of surface melting (Nagler and Rott, 2000; Liang et al., 2021; Li et al., 2023), suggesting that this is a reasonable empirical choice that is consistent with prior work on wet snow mapping with S-1. Figure 2c shows the five-year melt extent mosaic, with the region we consider for ice slab detection ($\Delta\sigma^0 < -4.7$ dB) highlighted in the blue.

To exclude firn aquifer regions, we use the Sentinel-1 firn aquifer map originally published in Brangers et al. (2020). These firn aquifer areas were detected by identifying pixels where the mean April σ_{HV}^0 exceeded the mean September σ_{HV}^0 by 9.4 dB or more, using mean monthly values aggregated over 2014-2019, similar to our firn saturation map. Figure 2d shows the locations of these firn aquifers in relation to previous OIB ice slab detections.

3.3 Threshold Optimization and Uncertainty Analysis

To map ice slabs with our S-1 mosaics, we optimize independent backscatter thresholds that demarcate the upper and lower limit of the ice slabs. For the upper boundary, we first take the σ_{HV}^0 and σ_{xpol}^0 mosaics and mask out the dry snow zone and firn aquifer regions. We then define ice slabs as covering the region where $\sigma_{HV}^0 < \alpha$ and $\sigma_{xpol}^0 < \beta$, where α and β are independent empirical thresholds. We search for the optimal values of α and β that maximize the agreement between the upper limit of the ice slabs as detected by airborne ice-penetrating radar, and the upper limit of the ice slabs as estimated by S-1.

To optimize α and β , we create a training data set using the Jullien et al. (2023) high-end estimate of ice slab extent derived from OIB flight lines surveyed in March-May 2017. For each flight line that passes through an ice slab area, we extract the portion of the flight line that overflies the ice slabs, as well as an additional 50 km buffer that extends inland of the upper limit of the ice slabs. We discretize these lines into points every 50 m and assign each point a value of 1 if an ice slab was detected in the OIB data at that location or 0 if no ice slab was detected. Similarly, we binarize our S-1 ice slab detections where a pixel value of 1 means an ice slab was detected and 0 means no ice slab was detected. We then test all combinations of thresholds for $-7.12 \text{ dB} < \beta < -2.37 \text{ dB}$ and $-13.6 \text{ dB} < \alpha < -2.1 \text{ dB}$, calculate the F1 score for each combination, and choose the threshold values that give the highest F1 score. The F1 score is a measure of the accuracy of a binary classification and is calculated following Equation 1. Figure 3 shows this optimization trade space with the optimal threshold combination shown in the white dot. We find that using both σ_{xpol}^0 and σ_{HV}^0 thresholds together leads to modestly better agreement with the OIB detections, compared to using only σ_{xpol}^0 . The optimal ice slab extent estimated using only σ_{xpol}^0 has an F1 score of 0.787, compared to an F1 score of 0.811 for the joint optimization. The optimal ice slab extent estimated using only σ_{HV}^0 has an F1 score of only

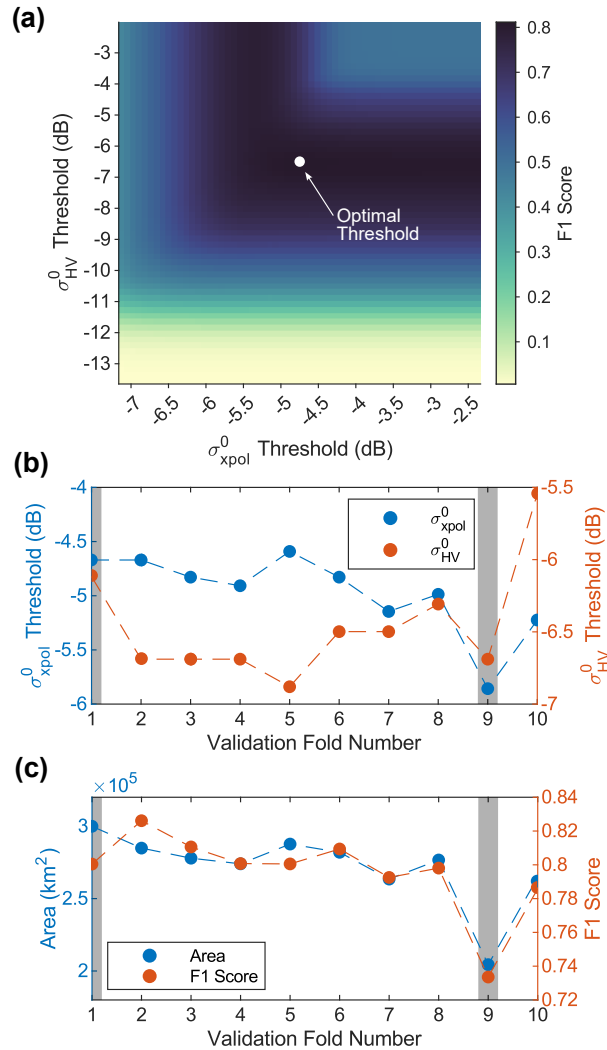


Figure 3. Optimization of the detection thresholds for the upper limit of ice slabs. a) F1 score as a function of σ_{xpol}^0 and σ_{HV}^0 thresholds. The optimal threshold combination (maximum F1 score) is shown in the white dot. b) Optimal thresholds from each iteration of the ten-fold cross validation scheme. The thresholds that give the minimum and maximum total ice slab extent are marked in the grey bars. We use these two thresholds to quantify uncertainty in the upper limit of the ice slabs. c) The total ice slab area and F1 score on the withheld validation set for each iteration of the ten-fold cross-validation.

0.674, so it is clear that the cross-polarized backscatter ratio provides significant additional information.

$$F1 = \frac{2 * \text{true positive}}{2 * \text{true positive} + \text{false positive} + \text{false negative}} \quad (1)$$

210 To quantify uncertainty in our detection of the upper limit of the ice slabs, we use a ten-fold cross-validation scheme. We divide our training dataset into ten even subsets, rerun our optimization routine on each data subset, and calculate the F1 score

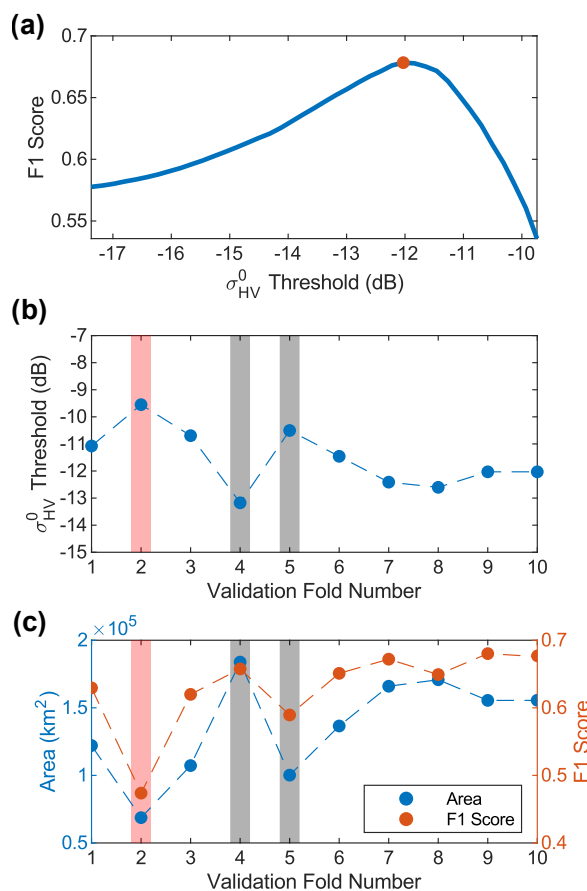


Figure 4. Optimization of the detection threshold, ϕ , for the lower limit of ice slabs. a) F1 score as a function of the σ_{HV}^0 threshold. The optimal threshold (maximum F1 score) is shown in the red dot. b) Optimal thresholds from each iteration of the ten-fold cross validation scheme. The thresholds that give the maximum and minimum total ice slab extent are marked in the grey bars. We use these two thresholds to quantify uncertainty in the lower limit of the ice slabs. c) The total ice slab area and F1 score on the withheld validation set for each iteration of the ten-fold cross-validation. We discard the iteration marked with the red bar to due to the anomalously poor F1 score and choose the maximum and minimum ice slab extents from the remaining nine iterations (marked in the two gray bars).

on the 90% of the data that was withheld. This yields ten separate estimates of the optimal backscatter thresholds, tuned to different regions of the ice sheet. We take the thresholds that yield the maximum and minimum total ice slab area and use these limits to bound the plausible extent of the ice slabs as estimated by S-1. Figure 3c-d shows the result of this analysis.

215 Next we separately optimize the threshold for detecting the lower boundary of the ice slabs using the same method as described above, but now using a training dataset that covers the ice slab region and a 50 km buffer down-flow into the ablation zone. Initial analysis of the backscatter mosaics suggests that σ_{xpol}^0 does not display any distinct change in behavior associated

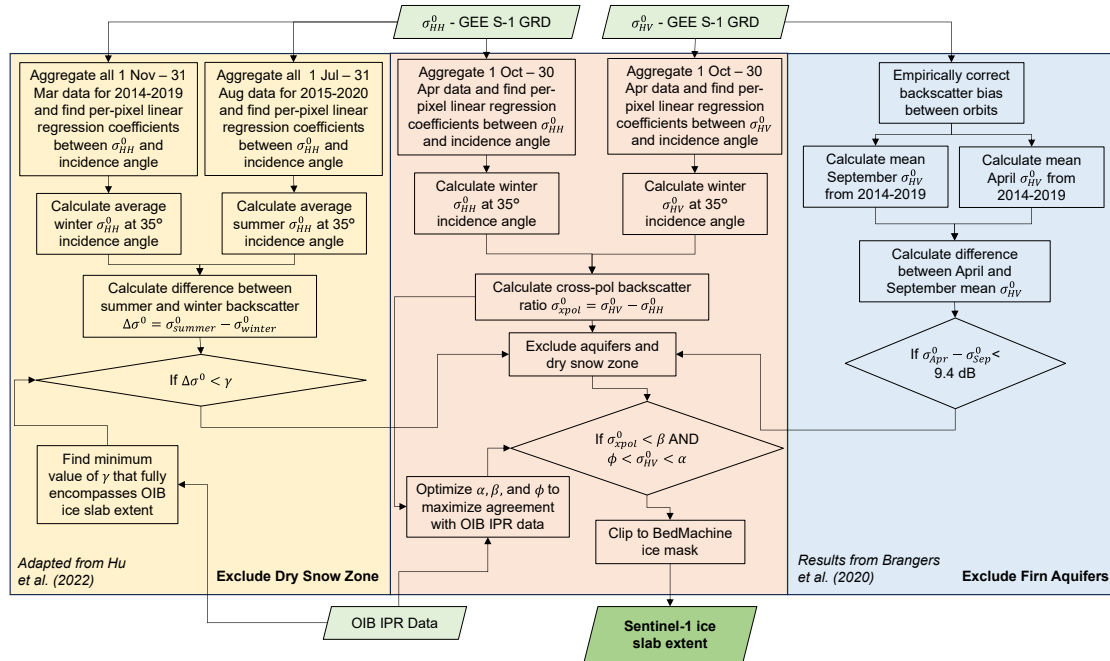


Figure 5. Sentinel-1 ice slab detection algorithm flowchart.

with the lower boundary (see Figure 1a), so we optimize a single threshold, $\sigma_{HV}^0 > \phi$, with uncertainty determined using the same ten-fold cross-validation scheme described above.

220 Finally, we use our optimized thresholds to map the minimum, most likely, and maximum extent of ice slabs from the S-1 data following the complete workflow shown in Figure 5. To quantify the accuracy of these mapped extents, we calculate the confusion matrix, F1 score, and Cohen’s κ for each limit.

4 Results and Discussion

4.1 Sentinel-1 Map of Ice Slab Extent

225 Figure 6 shows the S-1 estimated ice slab extent in winter 2016-2017, compared with the OIB ice slab detections. We find excellent agreement between the upper limit of the ice slabs as identified by OIB and the S-1 estimated upper limit. Figure 7 shows the confusion matrices, F1 scores, and Cohen’s κ for the minimum, most likely, and maximum S-1 estimated ice slab extent that quantify this agreement. The most likely ice slab extent has an F1 score of 0.811 with a true positive rate of 94% when detecting the upper limit of the ice slabs. The S-1 estimates at 500 m are also able to capture much of the km-scale
 230 variability along the upper limit, including regions of discontinuous ice slabs (see Figure 6f for an example). The fingering

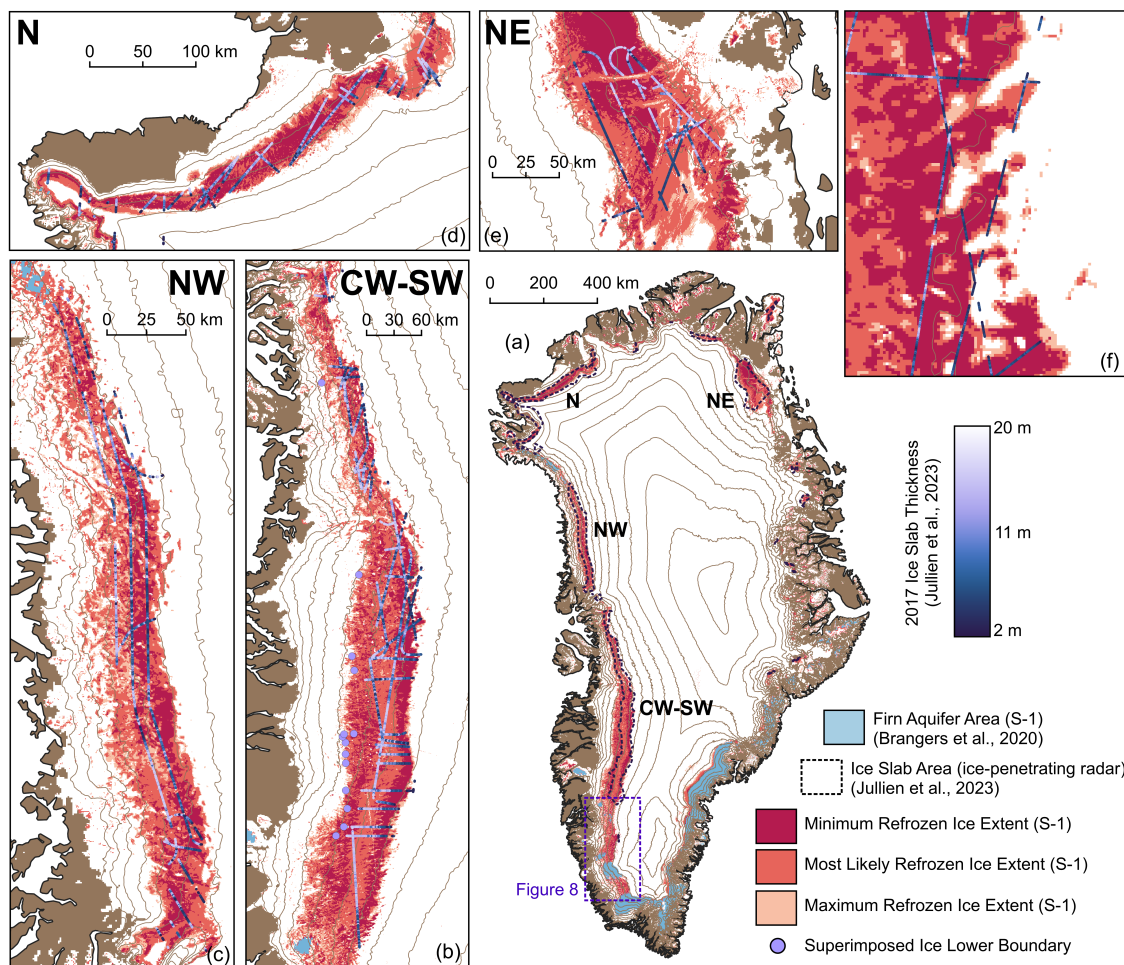


Figure 6. Sentinel-1 mapping of ice slabs in winter 2016-2017. a) S-1 detected ice slabs are shown in red, with the outline of the OIB detected ice slabs in the dashed black line (Jullien, 2023). We find overall excellent agreement between the S-1 and OIB mapping, although S-1 detects significant additional ice slab area in Southwest Greenland, along the Central East margin, and on peripheral ice caps. b) Zoom-in of the Central and Southwest regions. OIB ice slab detections are overlaid in the purple dots (Jullien, 2023), where darker colors indicated thinner ice slabs. There is a significant gap between the lower limit of the OIB ice slab detections and the lower limit of the S-1 mapping. The lower limit from S-1 is better aligned with the lower limit of superimposed ice as mapped from ice-penetrating radar in this paper (large purple dots). c) Zoom-in of Northwest region. d) Zoom-in of Northern region. e) Zoom-in of Northeast region. f) Zoom-in from Southwest Greenland showing details of the upper boundary. We find excellent agreement between the OIB and S-1 detections even where ice slabs are discontinuous due to preferential expansion in topographic lows. In all panels, the Greenland coastline was produced by the British Antarctic Survey (Gerrish, 2020), the ice mask as part of BedMachine v3 (Morlighem et al., 2017), and the 200 m contours are derived from ArcticDEM (Porter et al., 2018).

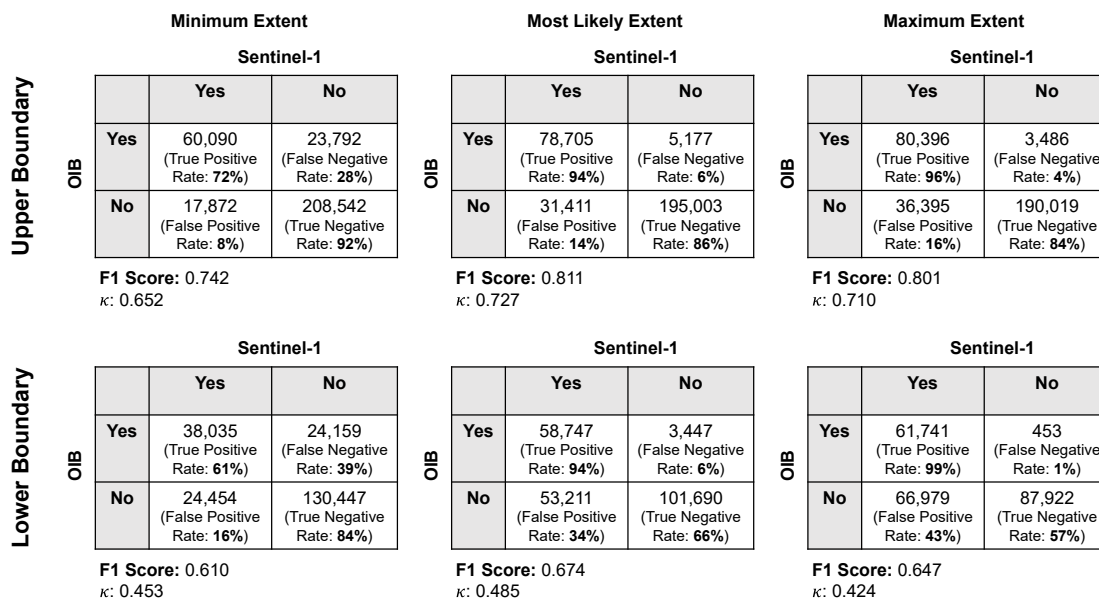


Figure 7. Confusion matrices quantifying the agreement between the OIB and S-1 ice slab detections for the minimum, maximum, and most likely ice slab extents. We quantify the fit for the upper boundary (top row) and lower boundary (bottom row) separately, since these thresholds were optimized separately. The most likely extent does an excellent job of detecting the upper limit of the ice slabs, with an F1 score of 0.811 and Cohen’s κ of 0.727, but the lower boundary is much more uncertain, with a best F1 score of only 0.674 and Cohen’s κ of 0.485, likely due to the consistent overestimation of ice slab extent in Southwest Greenland.

structures that we map in many regions are consistent with preferential expansion through topographic lows where water collects as it flows laterally through saturated firn layers.

Our mapping identifies new ice slab regions in Southwest Greenland that have not been previously classified as such, likely due to a lack of comprehensive airborne radar coverage in this region. These newly-identified ice slab areas are highly consistent with the extent of the visible runoff zone mapped from Landsat imagery in Tedstone and Machguth (2022), confirming that vertical percolation is limited in these areas (Figure 8). However, the S-1 ice slab extent is often patchy and discontinuous in this region, likely due to the high prevalence of buried surface lakes and isolated aquifer regions that limit detection of ice slabs due to the presence of liquid water in the subsurface.

There are also a number of discrepancies between the OIB and S-1 mapping. In the northwest, S-1 appears to slightly underestimate the upper elevation of the ice slabs, particularly where they transition to firn aquifers, and the ice slab extent is fairly discontinuous in this region. The S-1 algorithm generally fails to detect ice slabs in basins with persistent buried supraglacial lakes because surface scattering from the water table dominates the return, likely contributing to this discontinuous mapping in the Northwest where buried lakes are common (Koenig et al., 2015). In the Northeast, the S-1 algorithm fails to detect gaps in the ice slabs in the shear margins of the Northeast Greenland Ice Stream that are present in the OIB data. This

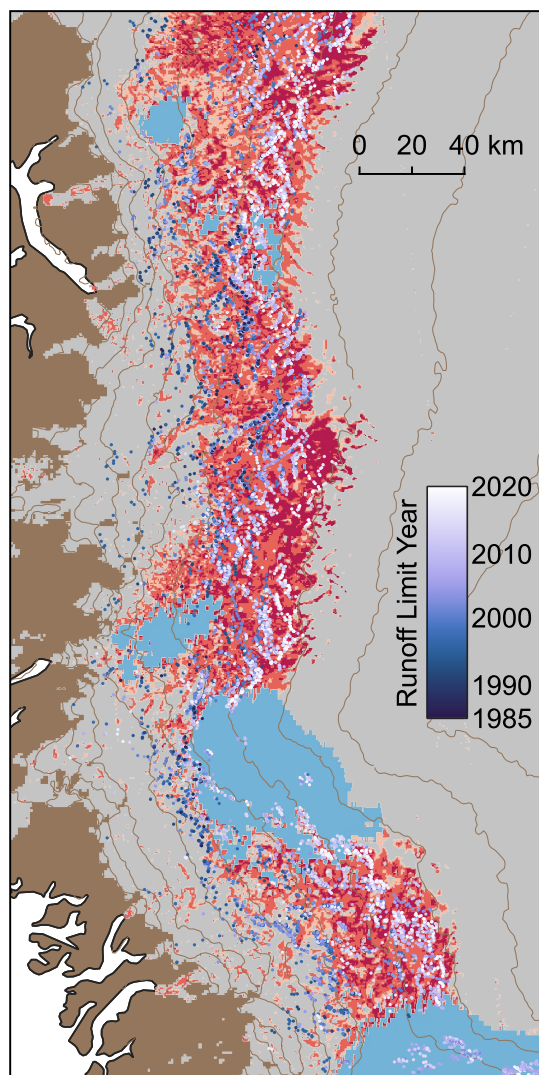


Figure 8. Comparison of the maximum visible runoff line from 1985-2020 with the newly mapped ice slabs regions in Southwest Greenland. The ice slab regions are marked with the same orange and red color scheme as Figure 6 and firn aquifers are shown in light blue (Brangers et al., 2020). Points marking the visible runoff limit in each sector, color-coded by year of observation, are overlaid in purple (Tedstone, 2022). There is a clear correspondence between the newly mapped ice slab regions and the runoff limit, confirming that vertical percolation is limited in these areas. The Greenland coastline was produced by the British Antarctic Survey (Gerrish, 2020), the ice mask as part of BedMachine v3 (Morlighem et al., 2017), and the 200 m contours are derived from ArcticDEM (Porter et al., 2018).

245 highlights that regions with significant surface crevassing are challenging for both OIB and S-1 detection of ice slabs. S-1 will tend to overestimate ice slab extent in crevassed regions, due to enhanced σ_{HV}^0 that our algorithm ascribes to volume scattering from firn, but actually results from rough surface and multi-bounce effects within the crevasses. On the other hand,



surface crevasse clutter in the OIB data can prevent definitive classification of the near-surface structure, particularly when using radiometric metrics that assume relatively homogeneous planar structures. The S-1 algorithm also fails to detect some isolated ice slab segments identified at anomalously high elevations in the OIB data in the North and Northwest. Manual review of the radargrams in these areas shows that most fall in high melt, high accumulation areas where a thick layer of relatively transparent winter snow overlying a strong reflector at the previous summer surface may have been misclassified as an ice slab.

We also consistently map ice slabs along the upper boundaries of firn aquifer, both in the Northwest and Southeast, that are not identified in the OIB data. It is possible that these areas represent aquifer regions with low volumetric water content where the seasonal backscatter variability does not meet the threshold for aquifer detection, but surface scattering is still enhanced by partial winter meltwater retention. Time series of σ_{HV}^0 from these aquifer-marginal areas in the Southeast show an intermediate scattering regime, with slower backscatter recovery than the percolation zone, but more rapid recovery than the well-defined aquifer regions. Alternately, there is ice-penetrating radar evidence for near-surface refreezing in continuous ice layers less than 1 m thick following both the 2012 and 2015 melt seasons (Culberg et al., 2021; Miller et al., 2022a) that extend to the upper limit of the southeastern firn aquifers. Similar shallow ice layers might also contribute to enhanced surface scattering and lead to erroneous ice slab detections in the Southeast.

Overall, we estimate a most likely ice slab extent of 104,020 km², compared to previous estimates of 60,400 - 73,500 km² from OIB data processed in Jullien et al. (2023) and 76,000 km² from SMAP data processed in Miller et al. (2022a). Much of this additional area comes from the newly detected regions in Southwest Greenland, as well as smaller contributions from narrow regions along the periphery, peripheral ice caps including Flade Isblink, and some misclassified regions at lower elevations and in fast-flowing glacier tongues in the mountainous eastern basins. Difficulty in accurately mapping the lower boundary of the ice slabs, further discussed in Section 4.2, also adds to the discrepancy in total extent.

4.2 Uncertainty in the Lower Boundary of Ice Slabs

Mapping the lower elevation limit of ice slabs is significantly more challenging than mapping the upper limit, as evidenced by the large uncertainty and apparently poor fit with the OIB detections. Our best estimate of the lower limit of the ice slabs has an F1 score of 0.674, compared to 0.811 for the upper boundary. There are two major sources of uncertainty which may contribute to this poor fit. First, it is likely that the limited penetration depth of S-1 prevents a clear delineation between regions where ice slabs are simply thicker than the system depth sensitivity and regions with a solid ice column. Figure 9 shows two-dimensional histograms of S-1 backscatter versus OIB-detected ice slab thickness. Both σ_{HV}^0 and σ_{xpol}^0 show little to no relationship with ice slab thickness beyond ~ 7 m, suggesting that S-1 is largely insensitive to scattering structure below that depth. Since well-developed ice slabs in regions such as Southwest Greenland are often 8-10 m thick, it is unsurprising that S-1 struggles to clearly detect the transition from ice slabs to solid ice. Second, the lower limit of the ice slabs in the airborne ice-penetrating radar dataset is not actually a data-driven boundary. Jullien et al. (2023) used the RACMOv2.3p regional climate model to exclude any regions below the long-term equilibrium line from their analysis, so the lower boundary is actually set by the model results. Given the simple snow model coupled to RACMO, the model may not accurately capture the true extent of ice slabs. Additionally, it almost certainly does not capture complex regions where near-surface ice may have been formed by

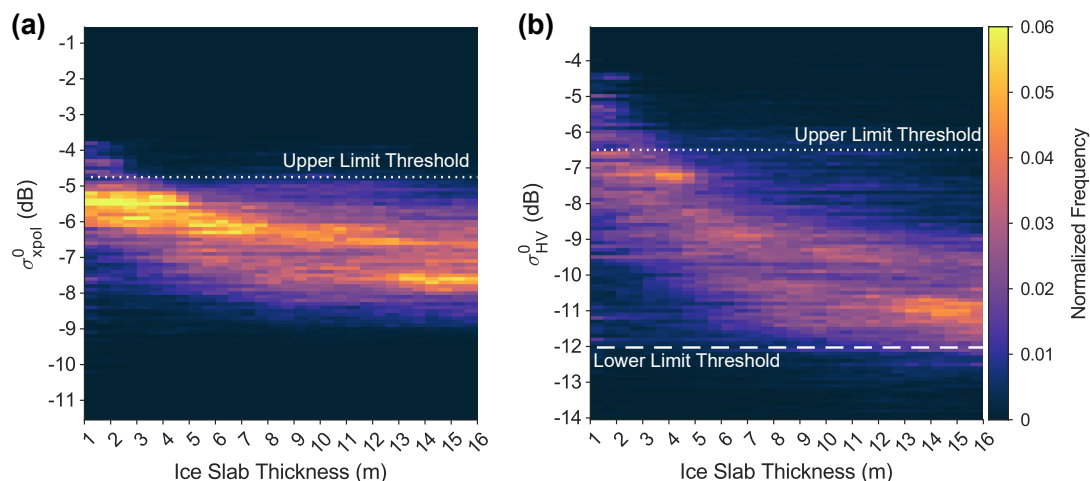


Figure 9. Sentinel-1 backscatter sensitivity to subsurface structure. a) Normalized two-dimensional histogram of ice slab thickness from ice-penetrating radar versus Sentinel-1 σ_{xpol}^0 . b) Normalized two-dimensional histogram of ice slab thickness from ice-penetrating radar versus Sentinel-1 σ_{HV}^0 . In both cases, the change in backscatter saturates around an ice slab thickness of ~ 7 m, suggesting that the S-1 penetration depth is limited to approximately that depth. The optimal thresholds for the upper and lower limit of the ice slabs are shown in dashed white lines on each plot. This figure also demonstrates that the σ_{xpol}^0 metric improves detection of the ice slab upper limit because the spread of backscatter values that map to an ice slab thickness of 1-2 m is significantly reduced compared to σ_{HV}^0 .

refreezing, even if firn is no longer present. This includes historical ice slab regions, superimposed ice regions, where meltwater fully saturates the annual accumulation and refreezes to form surface ice layers (Benson, 1962), areas where the firn column may have been completely filled by surface meltwater draining through surface crevasses (Culberg et al., 2022a), or regions
285 where refrozen ice was advected in from higher elevations.

We hypothesize that any ice formed by refreezing induces significant volume scattering due to trapped air bubbles, interstitial firn pockets, and other heterogeneities in density, leading to a σ_{HV}^0 signature that is more similar to ice slabs than meteoric ice. This is consistent with previous work which showed clear differences in C-band polarimetric backscatter between glacier ice, superimposed ice, and firn regions (Langley et al., 2008, 2009; Barzycka et al., 2019). To test this hypothesis, we reanalyze
290 14 airborne radar data flights from 2017 in Central West and Southwest Greenland that are approximately parallel to ice flow. Both the IMAU Firn Densification model (Brils et al., 2022) and the maximum depth of ice blobs observed in the Jakobshavn catchment (Culberg et al., 2022a) suggest that pore close-off occurs at around 30 m depth in this region. Therefore, in each radargram, we identify an englacial layer that is approximately 30 m below the surface near the upper limit of the ice slabs and assume it represents the bottom of the firn column. We trace this layer downstream until it outcrops at the surface due
295 to ablation. Where surface sidelobes obscure the radiostratigraphy or there are significant stratigraphic disturbances near the surface, we estimate the maximum outcropping elevation as the last point where the layer can be clearly traced, and the minimum elevation as the point where we would extrapolate the layer outcropping to occur if the layer slope remained the

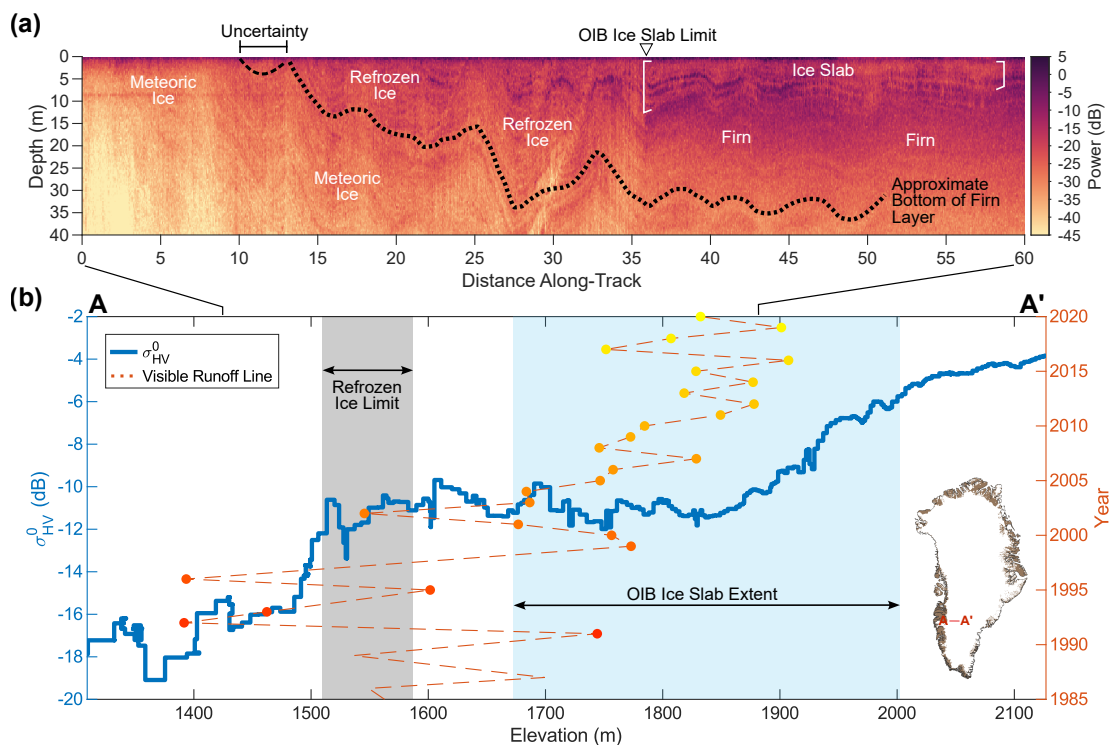


Figure 10. Sentinel-1 detects the lower limit of refrozen ice facies. (Contains modified Copernicus Sentinel data 2016-2017, processed by ESA.) a) Accumulation Radar transect from April 2017 (Paden et al., 2014b) showing the inferred transition from ice slabs, to superimposed ice facies, to solid meteoric ice. The dashed black line shows the englacial layer that we trace from the bottom of the firn until it outcrops at the surface in order to define the lower limit of the refrozen ice facies. b) Comparison of σ_{HV}^0 (blue line) as a function of elevation with the OIB ice slab extent (blue patch) (Jullien, 2023), estimated lower boundary of superimposed ice facies (grey patch, this paper), and the elevation of the visible runoff line between 1985 and 2020 (dashed red line with dots at annual measurement points) (Tedstone, 2022). The region where we infer that surface ice was formed by refreezing is marked by a plateau in σ_{HV}^0 around -11 dB and is also the region over which the visible runoff zone has retreated in the last two decades, supporting the idea that this region may have been near or above the firn-line in the recent past. The inset map in panel b (Gerrish, 2020; Morlighem et al., 2017) shows the location of this transect in Southwest Greenland.

same. Figure 10a shows an example of this layer tracing process. We infer that ice at depths shallower than the traced layer was likely formed by refreezing, rather than compaction.

300 In Figure 6b, the large purple dots mark the minimum elevations of these outcropping points, showing strong agreement between the S-1 inferred lower boundary of ice slabs and this new OIB-inferred limit of refrozen surface ice facies. This region between the boundary of refrozen ice facies and the lower limit of the OIB-mapped ice slabs corresponds to the area over which the visible runoff line has retreated since the mid-1980s (see Figure 10) (Tedstone and Machguth, 2022), with significant interannual variability in runoff extent. This suggests that the S-1 mapping in part captures the historical equilibrium



305 zone, which would have been in positive mass balance prior to the 1980s and may have still experienced intermittent years of positive mass balance into the early 1990s. Given the slow ice flow in the Southwest ($\sim 40 \text{ ma}^{-1}$), this contributes to a wide zone where surface ice consists of historical ice slabs that have not yet fully ablated, further modified by intermittent superimposed ice formation, and ongoing downstream advection of other refrozen ice. Therefore, we infer that our S-1 mapping captures not only ice slabs, but all regions where the near-surface ice was formed predominantly by refreezing.

310 This conclusion is consistent with some of the regional differences in the mismatch between the S-1 and OIB-inferred lower extent of the ice slabs. In the Southwest, there is a 20-35 km gap between the bottom of the OIB-detected ice slabs and S-1 mapped ice slabs. This is consistent with the low surface slopes, long history of melt, and slow and variable retreat of the snowline and expansion of the visible runoff zone in this region (Ryan et al., 2019; Tedstone and Machguth, 2022). In contrast, the two mappings agree fairly well in the North which has seen consistent expansion of the runoff zone and retreat of the snowline since 1990 (Ryan et al., 2019; Noël et al., 2019), suggesting that the formation of refrozen ice facies in this region is a more recent and rapid phenomenon. However, some of the discrepancies in the lower limit are likely attributable to other complex surface scattering mechanisms rather than an extended superimposed ice zone. For example, in the Northwest, the S-1 lower limit is particularly diffuse, with complicated and disconnected regions identified as potential refrozen ice all the way to the ice sheet margin. We hypothesize that this is due to a propensity for regions of heavy crevasses to be misclassified as refrozen ice, an issue which is more pronounced in the fast-flowing Northwest where surface strain rates are high and crevassing is prevalent.

4.3 Comparison with SMAP-Derived Extent

Figure 11 compares our S-1 derived refrozen ice facie extent with the ice slab extent derived from SMAP in Miller et al. (2022a). Overall, S-1 offers a significant improvement in both accuracy and resolution, particularly capturing regions in Northwest Greenland that SMAP failed to classify as ice slabs and accurately capturing the elevation bands where ice slabs form in the North and Northeast. However, SMAP does a somewhat better job of capturing the lower limit of the ice slabs in Southwest Greenland, in large part because the lower limit of the SMAP-inferred percolation zone (dark purple dashed outline) is much more consistent with MODIS-inferred estimates of the summer snowline (Ryan et al., 2019) than S-1 (lilac region), which maps wet snow well into the ablation zone in some regions. SMAP also maps melt significantly further inland on the ice sheet than S-1, in part due to the comparatively coarse effective resolution, all of which contributes to different areas in which ice slabs are assumed to be viable.

The upcoming launch of the joint NASA-ISRO NISAR mission and eventual launch of ESA's Radar Observing System for Europe-L-Band (ROSE-L) mission will soon provide L-band synthetic aperture radar data over Greenland, which has the potential to offer the best of both these products. The enhanced penetration depth at L-band may particularly enable a better delineation of the low-elevation transition from ice slabs to superimposed ice and enable more robust constraints on ice slab thickness from space. The longer wavelength will also significantly improve interferometric coherence over the ice sheet and potentially enable ice slab mapping based on volume decorrelation (Rizzoli et al., 2017) or other coherence-derived metrics. This will be a particularly important avenue of investigation given NISAR is expected to primarily collect data in

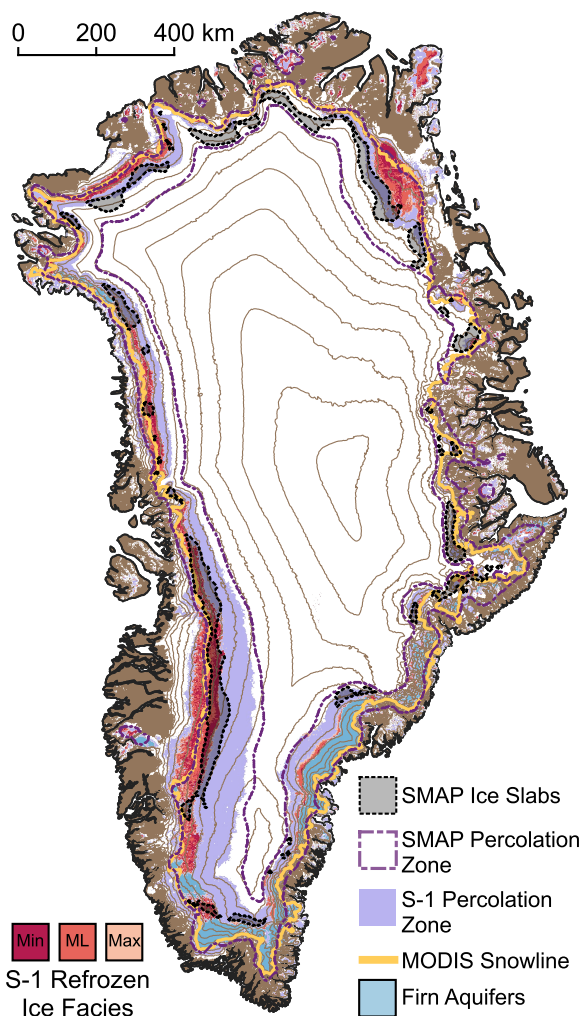


Figure 11. Comparison of S-1 inferred refrozen ice facies in winter 2016-2017 (this paper) and SMAP-inferred average ice slab extent from 2015-2019 (Miller, 2021). S-1 shows a significant improvement in resolution and accuracy over SMAP. However, SMAP is able to better capture the true extent of the percolation zone, and hence the lower limit of the ice slabs, as demonstrated by the better match between the lower limit of the SMAP-derived percolation zone (Miller, 2021) and a MODIS-derived estimate of the average summer snowline (Ryan et al., 2019). Firm aquifers are shown in light blue (Brangers et al., 2020).

single-polarization mode over Greenland. Additionally, NISAR will not collect data above 77.5° north, unfortunately limiting
340 future capacity to study the rapidly changing northern basins. However, where data are collected, these complementary L-band
observations have the potential to significantly improve our capacity to study the near-surface of Greenland from space, and
our C-band algorithm development will provide an important bridge between the historical OIB data and future L-band data,
which will not overlap in time with OIB.



5 Conclusions

345 We have shown that Sentinel-1 winter σ_{xpol}^0 and σ_{HV}^0 signatures can be used to map the extent of Greenland's refrozen ice
facies from space at 500 m spatial resolution. Our mapping is in excellent agreement with both subsurface observations from
the OIB ice-penetrating radar data and remote sensing observations of visible surface runoff. We identify new ice slab regions in
Southwest Greenland and our mapping suggests that ice slabs are largely ubiquitous in the wet snow zone in all regions besides
Southeast Greenland. Given the radiometric stability and consistent calibration efforts for Sentinel-1, we expect that it may be
350 possible to apply the optimized thresholds we derive here for winter 2016-2017 to data collected in other years. However, there
is still significant work to be done to assess the interannual radiometric stability of S-1 across the GrIS at various signal-to-
noise ratios and to characterize other forms of instrumental uncertainty, particularly due to the evolving observation strategy
of S-1 and missing measurements from either S-1A or S-1B in various years. Additionally, evolving conditions on the GrIS,
particularly in response to extreme melt (Culberg et al., 2021) and increasing rainfall (Box et al., 2022, 2023), may significantly
355 alter the subsurface stratigraphy, and therefore the observed backscatter, in ways that are not yet well-understood. Further work
in required to fully characterize the physical and dielectric mechanisms that drive C-band sensitivity to firn, ice slabs, and
superimposed ice structure and how their radiometric signatures may change with time. Future work might also focus on
improving the discrimination of crevasses and buried or drained lakes, which can currently lead to misclassifications in ice slab
regions. Regardless, the algorithm we develop here lays the groundwork for generating long time series of ice slab expansion
360 from C-band SAR observations with sufficient spatial coverage and resolution to enable long-term monitoring and validation
of predictive numerical models.

Data availability. Final Sentinel-1 mosaics (shown in Figure 2) and the final ice slab extent in winter 2016-2017 will be deposited at the
NSF Arctic Data Center with a permanent DOI at the time of manuscript acceptance. For the purposes of peer review, the current data
sets are temporarily available at: <https://drive.google.com/drive/folders/17NzLt60h8iWwQ8JP72mBsYaNFjLhOesx?usp=sharing> [Last Ac-
365 cess: 2023-11-08]. All Sentinel-1 data were accessed and processed through Google Earth Engine. The data catalog entry can be found at
https://developers.google.com/earth-engine/datasets/catalog/COPERNICUS_S1_GRD [Last Access: 2023-11-08]. Ice-penetrating radar de-
tections of slabs are available at <https://doi.org/10.5281/zenodo.7505426> [Last Access: 2023-11-08] (Jullien, 2023). Ice-penetrating radar
survey lines and the radargrams shown in Figures 1 and 10 are available from the Center for Remote Sensing and Integrated Systems at
<https://data.cresis.ku.edu/data/accum/> or through the National Snow and Ice Data Center at <https://nsidc.org/data/iracc1b/versions/2> [Last
370 Access: 2023-11-08] (Paden et al., 2014a, b). The elevation of the visible runoff line as a function of time is available at <https://zenodo.org/records/6472348> [Last Access: 2023-11-08] (Tedstone, 2022). Sentinel-1 firn aquifer detections are available at <https://arcticdata.io/catalog/view/doi%3A10.18739%2FA2HD7NS8N> [Last Access: 2023-11-08] (Brangers et al., 2020). The data used for throughout this paper for
basemaps of Greenland are available as follows. The Greenland coastline is available from the British Antarctic Survey at <https://data.bas.ac.uk/full-record.php?id=GB/NERC/BAS/PDC/01439> [Last Access: 2023-11-08] (Gerrish, 2020). The ice mask is available through BedMachine
375 Greenland v4 <https://sites.ps.uci.edu/morlighem/dataproducts/bedmachine-greenland/> [Last Access: 2023-11-08] (Morlighem et al., 2017).
The 200 m elevation contours are derived from ArcticDEM and available at <https://www.pgc.umn.edu/data/arcticdem/> [Last Access: 2023-
11-08] (Porter et al., 2018).

<https://doi.org/10.5194/egusphere-2023-2652>

Preprint. Discussion started: 1 December 2023

© Author(s) 2023. CC BY 4.0 License.



Author contributions. RC conceived the study, designed and implemented the processing algorithms, and wrote the initial paper draft. RJM and JZM provided guidance and suggestions on the Sentinel-1 processing and ice slab detection workflow. All authors contributed to the scientific analysis of results and writing of the final manuscript.

380

Competing interests. The contact author has declared that none of the authors has any competing interests.

Acknowledgements. JZM was supported by NASA grants 80NSSC20K1806 and 80NSSC18K1055.



References

- Agency, E. S.: Sentinel-1 SAR User Guide, Tech. rep.
- 385 Ashcraft, I. and Long, D.: Observation and Characterization of Radar Backscatter over Greenland, *IEEE Transactions on Geoscience and Remote Sensing*, 43, 225–237, <https://doi.org/10.1109/TGRS.2004.841484>, 2005.
- Ashcraft, I. S. and Long, D. G.: Comparison of Methods for Melt Detection over Greenland Using Active and Passive Microwave Measurements, *International Journal of Remote Sensing*, 27, 2469–2488, <https://doi.org/10.1080/01431160500534465>, 2006.
- Bader, H.: Sorge’s Law of Densification of Snow on High Polar Glaciers, *Journal of Glaciology*, 2, 319–323,
390 <https://doi.org/10.3189/S0022143000025144>, 1954.
- Barzycka, B., Błaszczyk, M., Grabciec, M., and Jania, J.: Glacier Facies of Vestfonna (Svalbard) Based on SAR Images and GPR Measurements, *Remote Sensing of Environment*, 221, 373–385, <https://doi.org/10.1016/j.rse.2018.11.020>, 2019.
- Baumgartner, F., Jezek, K. C., Forster, R. R., Gogineni, S. P., and Zabel, I. H. H.: Spectral and Angular Ground-Based Radar Backscatter Measurements of Greenland Snow Facies, in: 1999 IGARSS, 614, pp. 1053–1055, Hamburg, Germany,
395 <https://doi.org/10.1109/IGARSS.1999.774530>, 1999.
- Benson, C. S.: Stratigraphic Studies in the Snow and Firm of the Greenland Ice Sheet, Doctoral Thesis, California Institute of Technology, 1962.
- Box, J. E., Wehrlé, A., van As, D., Fausto, R. S., Kjeldsen, K. K., Dachauer, A., Ahlstrøm, A. P., and Picard, G.: Greenland Ice Sheet Rainfall, Heat and Albedo Feedback Impacts From the Mid-August 2021 Atmospheric River, *Geophysical Research Letters*, 49, e2021GL097356,
400 <https://doi.org/10.1029/2021GL097356>, 2022.
- Box, J. E., Nielsen, K. P., Yang, X., Niwano, M., Wehrlé, A., van As, D., Fettweis, X., Køltzow, M. A. Ø., Palmason, B., Fausto, R. S., van den Broeke, M. R., Huai, B., Ahlstrøm, A. P., Langley, K., Dachauer, A., and Noël, B.: Greenland Ice Sheet Rainfall Climatology, Extremes and Atmospheric River Rapids, *Meteorological Applications*, 30, e2134, <https://doi.org/10.1002/met.2134>, 2023.
- Brangers, I., Lievens, H., Miège, C., Demuzere, M., Brucker, L., and De Lannoy, G. J.: Sentinel-1 Detects Firm Aquifers in the Greenland
405 Ice Sheet, *Geophysical Research Letters*, 47, <https://doi.org/10.1029/2019GL085192>, 2020.
- Brils, M., Kuipers Munneke, P., Van De Berg, W. J., and Van Den Broeke, M.: Improved Representation of the Contemporary Greenland Ice Sheet Firm Layer by IMAU-FDM v1.2G, *Geoscientific Model Development*, 15, 7121–7138, <https://doi.org/10.5194/gmd-15-7121-2022>, 2022.
- Culberg, R., Schroeder, D. M., and Chu, W.: Extreme Melt Season Ice Layers Reduce Firm Permeability across Greenland, *Nature Communications*, 12, 1–9, <https://doi.org/10.1038/s41467-021-22656-5>, 2021.
- Culberg, R., Chu, W., and Schroeder, D. M.: Shallow Fracture Buffers High Elevation Runoff in Northwest Greenland, *Geophysical Research Letters*, 49, <https://doi.org/10.1029/2022GL101151>, 2022a.
- Culberg, R., Lai, C.-Y., and Michaelides, R.: Ice-Penetrating Radar Observations of Ice Slab Development and Change, 2022b.
- Enderlin, E., Howat, I., Jeong, S., Noh, M.-J., van Angelen, J. H., and van de Broeke, M. R.: An Improved Mass Budget for the Greenland
415 Ice Sheet, *Geophysical Research Letters*, 41, 866–872, <https://doi.org/10.1002/2013GL059010>, 2014.
- Fahnestock, M. A., Bindshadler, R., Kwok, R., and Jezek, K.: Greenland Ice Sheet Surface Properties and Ice Dynamics from ERS-1 SAR Imagery, *Science*, 262, 1530–1534, 1993.



- Fischer, G., Jäger, M., Papathanassiou, K. P., and Hajnsek, I.: Modeling the Vertical Backscattering Distribution in the Percolation Zone of the Greenland Ice Sheet With SAR Tomography, *IEEE Journal of Selected Topics in Applied Earth Observations and Remote Sensing*, 12, 4389–4405, <https://doi.org/10.1109/JSTARS.2019.2951026>, 2019.
- 420 Forster, R. R., Box, J. E., Van Den Broeke, M. R., Miège, C., Burgess, E. W., Van Angelen, J. H., Lenaerts, J. T., Koenig, L. S., Paden, J., Lewis, C., Gogineni, S. P., Leuschen, C., and McConnell, J. R.: Extensive Liquid Meltwater Storage in Firn within the Greenland Ice Sheet, *Nature Geoscience*, 7, 95–98, <https://doi.org/10.1038/ngeo2043>, 2014.
- Fox-Kemper, B., Hewitt, H., Xiao, C., Aðalgeirsdóttir, G., Drijfhout, S. S., Edwards, T., Golledge, N., Hemer, M., Kopp, R., Krinner, G., 425 Mix, A., Notz, D., Nowicki, S., Nurhati, I., Ruiz, L., Sallée, J.-B., Slangen, A., and Yu, Y.: Ocean, Cryosphere and Sea Level Change. In *Climate Change 2021: The Physical Science Basis*, in: Intergovernmental Panel on Climate Change Sixth Assessment Report, chap. Chapter 9, pp. 1211–1362, <https://doi.org/10.1017/9781009157896.011.1212>, 2021.
- Gerrish, L.: The Coastline of Kalaallit Nunaat/ Greenland Available as a Shapefile and Geopackage, Covering the Main Land and Islands, with Glacier Fronts Updated as of 2017, <https://doi.org/10.5285/8cecd06-8474-4b58-a9cb-b820fa4c9429>, 2020.
- 430 Gorelick, N., Hancher, M., Dixon, M., Ilyushchenko, S., Thau, D., and Moore, R.: Google Earth Engine: Planetary-scale Geospatial Analysis for Everyone, *Remote Sensing of Environment*, 202, 18–27, <https://doi.org/10.1016/j.rse.2017.06.031>, 2017.
- Harper, J., Humphrey, N., Pfeffer, W. T., Brown, J., and Fettweis, X.: Greenland Ice-Sheet Contribution to Sea-Level Rise Buffered by Meltwater Storage in Firn, *Nature*, 491, 240–243, <https://doi.org/10.1038/nature11566>, 2012.
- Harper, J., Saito, J., and Humphrey, N.: Cold Season Rain Event Has Impact on Greenland’s Firn Layer Comparable to Entire Summer Melt 435 Season, *Geophysical Research Letters*, 50, e2023GL103 654, <https://doi.org/10.1029/2023GL103654>, 2023.
- Herron, M. M. and Langway, C. C.: Firn Densification: An Empirical Model, *Journal of Glaciology*, 25, 373–385, <https://doi.org/10.3189/s0022143000015239>, 1980.
- Hicks, B. R. and Long, D. G.: Inferring Greenland Melt and Refreeze Severity from SeaWinds Scatterometer Data, *International Journal of Remote Sensing*, 32, 8053–8080, <https://doi.org/10.1080/01431161.2010.532174>, 2011.
- 440 Hoen, W.: A Correlation-Based Approach to Modeling Interferometric Radar Observations of the Greenland Ice Sheet, Doctoral, Stanford University, 2001.
- Hu, J., Zhang, T., Zhou, X., Jiang, L., Yi, G., Wen, B., and Chen, Y.: Extracting Time-Series of Wet-Snow Facies in Greenland Using Sentinel-1 SAR Data on Google Earth Engine, *IEEE Journal of Selected Topics in Applied Earth Observations and Remote Sensing*, 15, 6190–6196, <https://doi.org/10.1109/JSTARS.2022.3192409>, 2022.
- 445 Humphrey, N. F., Harper, J. T., and Pfeffer, W. T.: Thermal Tracking of Meltwater Retention in Greenland’s Accumulation Area, *Journal of Geophysical Research: Earth Surface*, 117, 1–11, <https://doi.org/10.1029/2011JF002083>, 2012.
- Jezeq, K. C., Drinkwater, M. R., Crawford, J. P., Bindschadler, R., and Kwok, R.: Analysis of Synthetic Aperture Radar Data Collected over the Southwestern Greenland Ice Sheet, *Journal of Glaciology*, 39, 119–132, <https://doi.org/10.3189/S002214300001577X>, 1993.
- Jezeq, K. C., Gogineni, P., and Shanableh, M.: Radar Measurements of Melt Zones on the Greenland Ice Sheet, *Geophysical Research 450 Letters*, 21, 33–36, <https://doi.org/10.1029/93GL03377>, 1994.
- Jullien, N.: Data: Greenland Ice Sheet Ice Slab Expansion and Thickening, <https://doi.org/10.5281/zenodo.7505426>, 2023.
- Jullien, N., Tedstone, A. J., Machguth, H., Karlsson, N. B., and Helm, V.: Greenland Ice Sheet Ice Slab Expansion and Thickening, *Geophysical Research Letters*, 50, e2022GL100911, <https://doi.org/10.1029/2022GL100911>, 2023.



- Koenig, L. S., Lampkin, D. J., Montgomery, L. N., Hamilton, S. L., Turrin, J. B., Joseph, C. A., Moutsafa, S. E., Panzer, B., Casey, K. A.,
455 Paden, J. D., Leuschen, C., and Gogineni, P.: Wintertime Storage of Water in Buried Supraglacial Lakes across the Greenland Ice Sheet,
The Cryosphere, 9, 1333–1342, <https://doi.org/10.5194/tc-9-1333-2015>, 2015.
- Langley, K., Hamran, S. E., Høgda, K. A., Storvold, R., Brandt, O., Hagen, J. O., and Kohler, J.: Use of C-band Ground Penetrating
Radar to Determine Backscatter Sources within Glaciers, *IEEE Transactions on Geoscience and Remote Sensing*, 45, 1236–1245,
<https://doi.org/10.1109/TGRS.2007.892600>, 2007.
- 460 Langley, K., Hamran, S.-E., Hogda, K. A., Storvold, R., Brandt, O., Kohler, J., and Hagen, J. O.: From Glacier Facies to SAR Backscatter
Zones via GPR, *IEEE Transactions on Geoscience and Remote Sensing*, 46, 2506–2516, <https://doi.org/10.1109/TGRS.2008.918648>,
2008.
- Langley, K., Lacroix, P., Hamran, S. E., and Brandt, O.: Sources of Backscatter at 5.3 GHz from a Superimposed Ice and Firn Area Revealed
by Multi-Frequency GPR and Cores, *Journal of Glaciology*, 55, 373–383, <https://doi.org/10.3189/002214309788608660>, 2009.
- 465 Li, G., Chen, X., Lin, H., Hooper, A., Chen, Z., and Cheng, X.: Glacier Melt Detection at Different Sites of Greenland Ice Sheet Using
Dual-Polarized Sentinel-1 Images, *Geo-spatial Information Science*, 0, 1–16, <https://doi.org/10.1080/10095020.2023.2252034>, 2023.
- Liang, D., Guo, H., Zhang, L., Cheng, Y., Zhu, Q., and Liu, X.: Time-Series Snowmelt Detection over the Antarctic Using Sentinel-1 SAR
Images on Google Earth Engine, *Remote Sensing of Environment*, 256, 112 318, <https://doi.org/10.1016/j.rse.2021.112318>, 2021.
- Lindsley, R. D. and Long, D. G.: ASCAT and QuikSCAT Azimuth Modulation of Backscatter Over East Antarctica, *IEEE Geoscience and*
470 *Remote Sensing Letters*, 13, 1134–1138, <https://doi.org/10.1109/LGRS.2016.2572101>, 2016.
- Long, D. G. and Drinkwater, M. R.: Greenland Ice-Sheet Surface Properties Observed by the Seasat-A Scatterometer at Enhanced Resolution,
Journal of Glaciology, 40, 213–230, <https://doi.org/10.3189/S0022143000007310>, 1994.
- Long, D. G. and Miller, J. Z.: Validation of the Effective Resolution of SMAP Enhanced Resolution Backscatter Products, *IEEE Journal*
of Selected Topics in Applied Earth Observations and Remote Sensing, 16, 3390–3404, <https://doi.org/10.1109/JSTARS.2023.3260726>,
475 2023.
- MacFerrin, M. J., Machguth, H., van As, D., Charalampidis, C., Stevens, C. M., Heilig, A., Vandecrux, B., Langen, P. L., Mottram, R. H.,
Fettweis, X., van den Broeke, M. R., Pfeffer, W. T., Moussavi, M., and Abdalati, W.: Rapid Expansion of Greenland’s Low-Permeability
Ice Slabs, *Nature*, 573, 403–407, <https://doi.org/10.1038/s41586-019-1550-3>, 2019.
- Machguth, H., Macferrin, M., Van As, D., Box, J. E., Charalampidis, C., Colgan, W., Fausto, R. S., Meijer, H. A., Mosley-Thompson, E., and
480 Van De Wal, R. S.: Greenland Meltwater Storage in Firn Limited by Near-Surface Ice Formation, *Nature Climate Change*, 6, 390–393,
<https://doi.org/10.1038/nclimate2899>, 2016.
- Marsh, P. and Woo, M.-K.: Wetting Front Advance and Freezing of Meltwater within a Snow Cover: 1. Observations in the Canadian Arctic,
Water Resources Research, 20, 1853–1864, <https://doi.org/10.1029/WR020i012p01853>, 1984.
- Miller, J. Z.: SMAP-derived Perennial Firn Aquifer and Ice Slab Extents 2015–2019, <https://doi.org/10.5281/zenodo.8380493>, 2021.
- 485 Miller, J. Z., Culberg, R., Long, D. G., Shuman, C. A., Schroeder, D. M., and Brodzik, M. J.: An Empirical Algorithm to Map Perennial
Firn Aquifers and Ice Slabs within the Greenland Ice Sheet Using Satellite L-band Microwave Radiometry, *The Cryosphere*, 16, 103–125,
<https://doi.org/10.5194/tc-16-103-2022>, 2022a.
- Miller, J. Z., Long, D. G., Shuman, C. A., Culberg, R., Hardman, M. A., and Brodzik, M. J.: Mapping Firn Saturation Over Greenland Using
NASA’s Soil Moisture Active Passive Satellite, *IEEE Journal of Selected Topics in Applied Earth Observations and Remote Sensing*, 15,
490 3714–3729, <https://doi.org/10.1109/JSTARS.2022.3154968>, 2022b.



- Morlighem, M., Williams, C. N., Rignot, E., An, L., Arndt, J. E., Bamber, J. L., Catania, G., Chauche, N., Dowdeswell, J. A., Dorschel, B., Fenty, I., Hogan, K., Howat, I., Hubbard, A., Jakobsson, M., Jordan, T. M., Kjeldsen, K. K., Millan, R., Mayer, L., Mouginto, J., Noël, B. P. Y., O’Cofaigh, C., Palmer, S., Rysgaard, S., Seroussi, H., Siegert, M. J., Slabon, P., Straneo, F., van den Broeke, M. R., Weinrebe, W., Wood, M., Zinglensen, K. B., Chauché, N., Dowdeswell, J. A., Dorschel, B., Fenty, I., Hogan, K., Howat, I., Hubbard, A., Jakobsson, M., Jordan, T. M., Kjeldsen, K. K., Millan, R., Mayer, L., Mougintot, J., Noël, B. P., O’Cofaigh, C., Palmer, S., Rysgaard, S., Seroussi, H., Siegert, M. J., Slabon, P., Straneo, F., van den Broeke, M. R., Weinrebe, W., Wood, M., and Zinglensen, K. B.: BedMachine v3: Complete Bed Topography and Ocean Bathymetry Mapping of Greenland From Multibeam Echo Sounding Combined With Mass Conservation, *Geophysical Research Letters*, 44, 11,051–11,061, <https://doi.org/10.1002/2017GL074954>, 2017.
- Mougintot, J., Rignot, E., Bjørk, A. A., van den Broeke, M., Millan, R., Morlighem, M., Noël, B., Scheuchl, B., and Wood, M.: Forty-Six Years of Greenland Ice Sheet Mass Balance from 1972 to 2018, *Proceedings of the National Academy of Sciences of the United States of America*, 116, 9239–9244, <https://doi.org/10.1073/pnas.1904242116>, 2019.
- Munneke, P. K., M. Ligtenberg, S. R., van den Broeke, M. R., van Angelen, J. H., and Forster, R. R.: Explaining the Presence of Perennial Liquid Water Bodies in the Firn of the Greenland Ice Sheet, *Geophysical Research Letters*, 41, 476–483, <https://doi.org/10.1002/2013GL058389>, 2014.
- Nagler, T. and Rott, H.: Retrieval of Wet Snow by Means of Multitemporal SAR Data, *IEEE Transactions on Geoscience and Remote Sensing*, 38, 754–765, <https://doi.org/10.1109/36.842004>, 2000.
- Noël, B., van de Berg, W. J., Lhermitte, S., and van den Broeke, M. R.: Rapid Ablation Zone Expansion Amplifies North Greenland Mass Loss, *Science Advances*, 5, 2–11, <https://doi.org/10.1126/sciadv.aaw0123>, 2019.
- Paden, J., Li, J., Rodriguez-Morales, F., and Hale, R.: IceBridge MCoRDS Radar L1B Geolocated Radar Echo Strength Profiles, Version 2 [2015_Greenland_C130], <https://doi.org/10.5067/90S1XZRBAX5N>, 2014a.
- Paden, J., Li, J., Rodriguez-Morales, F., and Hale, R.: IceBridge Accumulation Radar L1B Geolocated Radar Echo Strength Profiles, Version 2 [2017_Greenland_P3], <https://doi.org/10.5067/0ZY1XYHNIQNY>, 2014b.
- Partington, K. C.: Discrimination of Glacier Facies Using Multi-Temporal SAR Data, *Journal of Glaciology*, 44, 42–53, <https://doi.org/10.3189/S0022143000002331>, 1998.
- Pfeffer, W. T. and Humphrey, N. F.: Formation of Ice Layers by Infiltration and Refreezing of Meltwater, *Annals of Glaciology*, 26, 83–91, <https://doi.org/10.3189/1998aog26-1-83-91>, 1998.
- Porter, C., Morin, P., Howat, I., Noh, M.-J., Bates, B., Peterman, K., Keesey, S., Schlenk, M., Gardiner, J., Tomko, K., Willis, M., Kelleher, C., Cloutier, M., Husby, E., Foga, S., Nakamura, H., Platson, M., Wethington, M., Williamson, C., Bauer, G., Enos, J., Arnold, G., Kramer, W., Becker, P., Doshi, A., D’Souza, C., Cummins, P., Laurier, F., and Bojesen, M.: ArcticDEM, V1, <https://doi.org/10.7910/DVN/OHHUKH>, 2018.
- Rignot, E.: Backscatter Model for the Unusual Radar Properties of the Greenland Ice Sheet, *Journal of Geophysical Research: Planets*, 100, 9389–9400, <https://doi.org/10.1029/95JE00485>, 1995.
- Rignot, E., Echelmeyer, K., and Krabill, W.: Penetration Depth of Interferometric Synthetic-Aperture Radar Signals in Snow and Ice, *Geophysical Research Letters*, 28, 3501–3504, <https://doi.org/10.1029/2000GL012484>, 2001.
- Rignot, E. J., Ostro, S. J., van Zyl, J. J., and Jezek, K. C.: Unusual Radar Echoes from the Greenland Ice Sheet, *Science*, 261, 1710–1713, <https://doi.org/10.1126/science.261.5129.1710>, 1993.
- Rizzoli, P., Martone, M., Rott, H., and Moreira, A.: Characterization of Snow Facies on the Greenland Ice Sheet Observed by TanDEM-X Interferometric SAR Data, *Remote Sensing*, 9, 315, <https://doi.org/10.3390/rs9040315>, 2017.



- Ryan, J. C., Smith, L. C., Van As, D., Cooley, S. W., Cooper, M. G., Pitcher, L. H., and Hubbard, A.: Greenland Ice Sheet Surface Melt Amplified by Snowline Migration and Bare Ice Exposure, *Science Advances*, 5, 1–11, <https://doi.org/10.1126/sciadv.aav3738>, 2019.
- 530 Swift, C. T., Hayes, P. S., Herd, J. S., Jones, W. L., and Delnore, V. E.: Airborne Microwave Measurements of the Southern Greenland Ice Sheet, *Journal of Geophysical Research: Solid Earth*, 90, 1983–1994, <https://doi.org/10.1029/JB090iB02p01983>, 1985.
- Tedesco, M. and Fettweis, X.: Unprecedented Atmospheric Conditions (1948–2019) Drive the 2019 Exceptional Melting Season over the Greenland Ice Sheet, *The Cryosphere*, 14, 1–26, <https://doi.org/10.5194/tc-2019-254>, 2020.
- 535 Tedstone, A.: Increasing Surface Runoff from Greenland’s Firn Areas, <https://doi.org/10.5281/zenodo.6472348>, 2022.
- Tedstone, A. J. and Machguth, H.: Increasing Surface Runoff from Greenland’s Firn Areas, *Nature Climate Change*, 12, 672–676, <https://doi.org/10.1038/s41558-022-01371-z>, 2022.
- Ulaby, F. T. and Long, D. G.: *Microwave Radar and Radiometric Remote Sensing*, The University of Michigan Press, Ann Arbor, MI, 2014.
- Van Den Broeke, M., Bamber, J., Ettema, J., Rignot, E., Schrama, E., Van Berg, W. J. D., Van Meijgaard, E., Velicogna, I., and Wouters, B.: 540 Partitioning Recent Greenland Mass Loss, *Science*, 326, 984–986, <https://doi.org/10.1126/science.1178176>, 2009.
- Vollrath, A., Mullissa, A., and Reiche, J.: Angular-Based Radiometric Slope Correction for Sentinel-1 on Google Earth Engine, *Remote Sensing*, 12, 1867, <https://doi.org/10.3390/rs12111867>, 2020.
- Wismann, V.: Monitoring of Seasonal Snowmelt on Greenland with ERS Scatterometer Data, *IEEE Transactions on Geoscience and Remote Sensing*, 38, 1821–1826, <https://doi.org/10.1109/36.851766>, 2000.